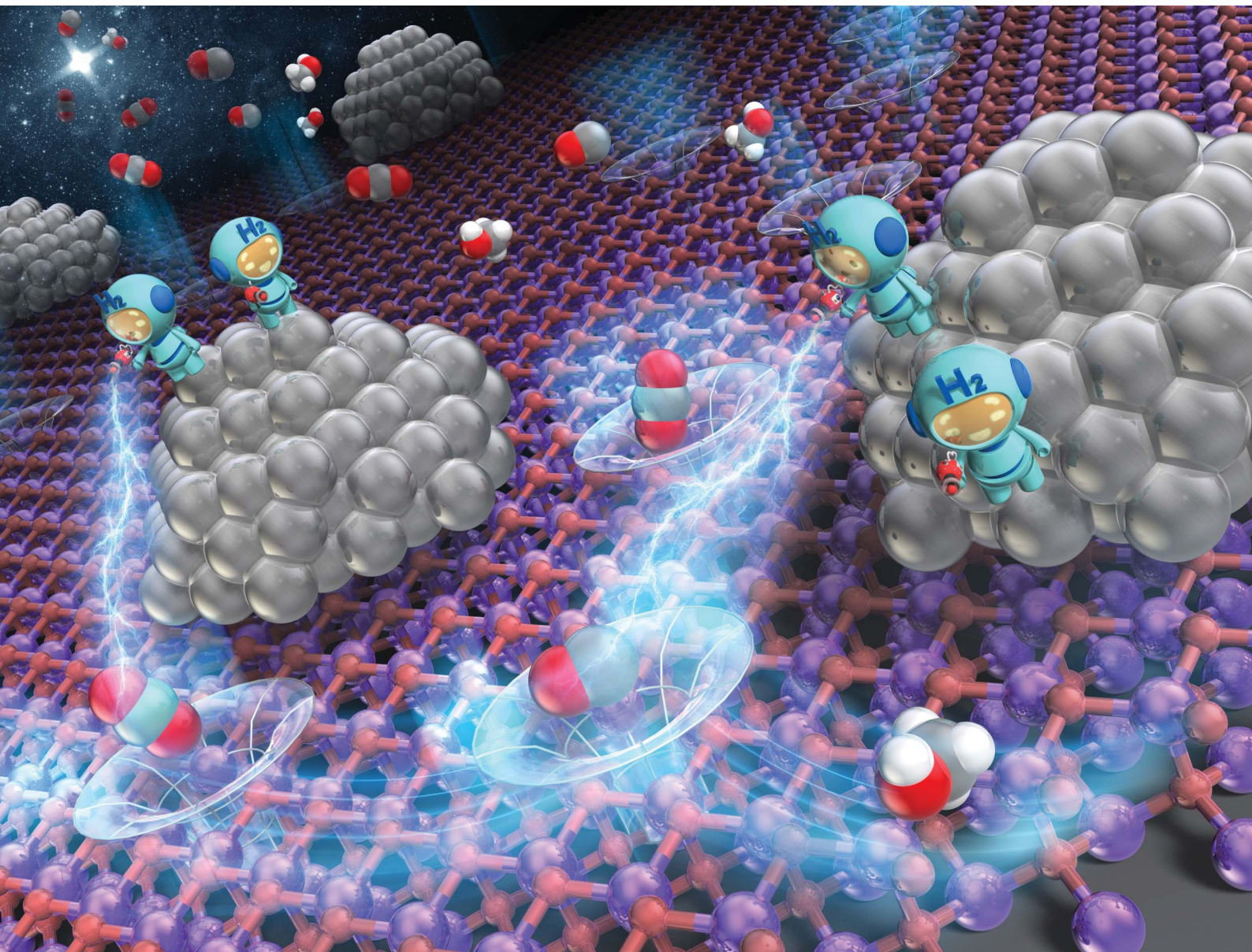


Chemical Science

rsc.li/chemical-science



ISSN 2041-6539

EDGE ARTICLE

Yasutaka Kuwahara, Hiromi Yamashita *et al.*
A quasi-stable molybdenum sub-oxide with abundant
oxygen vacancies that promotes CO_2 hydrogenation
to methanol



Cite this: *Chem. Sci.*, 2021, **12**, 9902

All publication charges for this article have been paid for by the Royal Society of Chemistry

A quasi-stable molybdenum sub-oxide with abundant oxygen vacancies that promotes CO₂ hydrogenation to methanol†

Yasutaka Kuwahara, ^{a,b,c,d} Takashi Mihogi, ^a Koji Hamahara, ^a Kazuki Kusu, ^a Hisayoshi Kobayashi ^{a,e} and Hiromi Yamashita ^{a,b,c}

Production of methanol from anthropogenic carbon dioxide (CO₂) is a promising chemical process that can alleviate both the environmental burden and the dependence on fossil fuels. In catalytic CO₂ hydrogenation to methanol, reduction of CO₂ to intermediate species is generally considered to be a crucial step. It is of great significance to design and develop advanced heterogeneous catalysts and to engineer the surface structures to promote CO₂-to-methanol conversion. We herein report an oxygen-defective molybdenum sub-oxide coupled with Pt nanoparticles (Pt/H_xMoO_{3-y}) which affords high methanol yield with a methanol formation rate of 1.53 mmol g_{-cat}⁻¹ h⁻¹ in liquid-phase CO₂ hydrogenation under relatively mild reaction conditions (total 4.0 MPa, 200 °C), outperforming other oxide-supported Pt catalysts in terms of both the yield and selectivity for methanol. Experiments and comprehensive analyses including *in situ* X-ray absorption fine structure (XAFS), *in situ* diffuse reflectance infrared Fourier transform (DRIFT) spectroscopy and density functional theory (DFT) calculations reveal that both abundant surface oxygen vacancies (V_O) and the redox ability of Mo species in quasi-stable H_xMoO_{3-y} confer the catalyst with enhanced adsorption and activation capability to subsequently transform CO₂ to methanol. Moreover, the Pt NPs act as H₂ dissociation sites to regenerate oxygen vacancies and as hydrogenation sites for the CO intermediate to finally afford methanol. Based on the experimental and computational studies, an oxygen-vacancy-mediated “reverse Mars–van Krevelen (M–vK)” mechanism is proposed. This study affords a new strategy for the design and development of an efficient heterogeneous catalyst for CO₂ conversion.

Received 9th May 2021
Accepted 26th June 2021

DOI: 10.1039/d1sc02550c
rsc.li/chemical-science

Introduction

The continuous accumulation of anthropogenic CO₂ in the atmosphere aggravates global warming. The control and reduction of CO₂ emissions have been a worldwide challenge and pressing issue. Carbon capture and storage (CCS) has been deemed as a promising technology to drastically reduce CO₂ emissions; however, appropriate carbon capture and utilization (CCU) technology must be developed to further reduce CO₂ emissions in a sustainable manner. Catalytic conversion of

anthropogenic CO₂ into valuable chemicals is regarded as a sustainable and appealing approach to alleviate simultaneously the environmental crisis and energy demands.^{1–4}

CO₂ is capable of being transformed to several important C1 chemicals such as CO, formic acid, methanol, and methane *via* hydrogenation.^{5–9} Among those, methanol (CH₃OH) has attracted huge interest from industries and scientific community, because it can be used as a raw material for the production of formalin, acetic acid, olefins, and gasoline, and can be utilized as a fuel molecule for automobiles and fuel cells.^{10,11} Methanol is currently produced from syngas (CO and H₂), generated by a steam reforming process using methane contained in liquefied natural gas (LNG) and petroleum gas (LPG), under extreme operational conditions (T = 240–260 °C, P = 5–10 MPa), in which Cu-based catalysts (e.g. Cu/ZnO/Al₂O₃) are used as a traditional catalyst.^{5,6,12,13} Production of methanol from anthropogenic CO₂ existing in the atmosphere or being discharged from large stationary sources *via* hydrogenation using CO₂-free H₂ produced by renewable energy sources would be a green chemical process that could alleviate both the environmental burden and the dependence on fossil fuels.^{14,15}

^aDivision of Materials and Manufacturing Science, Graduate School of Engineering, Osaka University, 2-1 Yamada-oka, Suita, Osaka 565-0871, Japan. E-mail: kuwahara@mat.eng.osaka-u.ac.jp; yamashita@mat.eng.osaka-u.ac.jp

^bInnovative Catalysis Science Division, Institute for Open and Transdisciplinary Research Initiatives (OTRI), Osaka University, 2-1 Yamada-oka, Suita, Osaka 565-0871, Japan

^cUnit of Elements Strategy Initiative for Catalysts & Batteries (ESICB), Kyoto University, Katsura, Kyoto 615-8520, Japan

^dJST, PRESTO, 4-1-8 Honcho, Kawaguchi, Saitama 332-0012, Japan

^eKyoto Institute of Technology, Matsugasaki, Sakyo-ku, Kyoto 606-8585, Japan

† Electronic supplementary information (ESI) available. See DOI: [10.1039/d1sc02550c](https://doi.org/10.1039/d1sc02550c)

Direct methanol synthesis from CO_2/H_2 *via* gas phase hydrogenation has been implemented industrially using supported Cu catalysts; however, a low equilibrium conversion of CO_2 at the operational conditions is seen as a bottleneck limiting large-scale operations. Methanol synthesis from CO_2/H_2 ($\text{CO}_2 + 3\text{H}_2 = \text{CH}_3\text{OH} + \text{H}_2\text{O}; \Delta H_{298}^0 = -49.5 \text{ kJ mol}^{-1}$) is an exothermic reaction, therefore, use of lower temperature and higher pressure conditions are thermodynamically more favorable.^{5,16} Recently, direct methanol synthesis in the liquid phase at lower temperatures has been studied, primarily because of easy control of the reaction temperature and easy extraction of products from the reaction system, which shifts the reaction equilibrium to the methanol production side.^{17,18} Although Ru-based homogeneous catalysts are known to function as active catalysts under relatively mild conditions, addition of additive reagents to achieve high reaction rates and problems associated with product separation and catalyst recovery are critical drawbacks.^{19–22} Alternatively, noble metal nanoparticle (NP) catalysts, such as Pt,^{23–27} Rh,^{28,29} and Re³⁰ *etc.* have been studied as heterogeneous catalysts for this reaction. In particular, Pt NPs are indispensable for the promotion of CO_2 hydrogenation due to the efficient donation of their d-orbital electrons into the π^* antibonding system of CO_2 . It has been reported that the activity of Pt NP catalysts is enhanced by manipulating the particle shape and the compositions (*e.g.* alloying with Co)^{23,24} or by the coupling with proper support material (*e.g.* MoS_2),²⁵ leading to a high methanol yield even at a low temperature of 150 °C.

In catalytic CO_2 hydrogenation, activation and cleavage of the stable C=O bond of CO_2 to form intermediate species is generally considered to be the crucial step. Previous literatures have reported the importance of an oxygen vacancy (V_O) of metal oxides in the activation of CO_2 .^{31,32} For example, Bobadilla *et al.* spectroscopically understood that the oxygen vacancies of TiO_2 support of Au/TiO_2 catalyst participate in reverse water-gas shift (RWGS) reaction by activating CO_2 .³³ Bhethanabotla and Kuhn *et al.* demonstrated that oxygen vacancy in $\text{La}_{0.75}\text{Sr}_{0.25}\text{FeO}_3$ perovskite-type oxide efficiently promotes CO_2 conversion in RWGS reaction.³⁴ Ge *et al.* demonstrated that the oxygen vacancy on the In_2O_3 surface assists CO_2 activation and hydrogenation and also stabilizes the key intermediates in CO_2 hydrogenation to methanol by using DFT calculation.³⁵ Previous studies demonstrated that oxygen vacancies formed in nonstoichiometric WO_{3-x} and MoO_{3-x} enable the light-assisted extraction of O atoms from CO_2 to form methane and CO, respectively.^{36,37} Thus, the assistance of oxygen vacancies in metal oxide is deemed as an appealing approach to activate molecular CO_2 and weaken the C=O double bond. However, because V_O sites are replenished by the dissociated O atoms during the reaction, the catalytic cycle cannot be realized. Coupling of V_O sites and metal particles that simultaneously activate H_2 to regenerate V_O sites is the key to sustaining a continuous catalytic cycle, which has been demonstrated extensively over oxide-supported metal catalysts.^{33,38–40} In this regard, our group reported that oxygen-defective molybdenum sub-oxide coupled with Pt NPs ($\text{Pt}/\text{H}_x\text{MoO}_{3-y}$) can function as a reusable catalyst for hydrodeoxygénéation of sulfoxide to produce sulfide under mild reaction conditions, in which

abundant oxygen vacancies in $\text{H}_x\text{MoO}_{3-y}$ act as the deoxygenation site and Pt NPs act as H_2 dissociation sites to continuously supply active H atoms for regenerating the oxygen vacancies.⁴¹ It is hypothesized that such a bifunctional catalytic system would be a viable catalyst for realizing simultaneous activation of CO_2 and H_2 and efficient hydrogenation of CO_2 to produce methanol.

In the present work, we report that an oxygen-defective molybdenum sub-oxide coupled with Pt NPs ($\text{Pt}/\text{H}_x\text{MoO}_{3-y}$) exhibits high methanol yield with a methanol formation rate of 1.53 $\text{mmol g}_{\text{cat}}^{-1} \text{h}^{-1}$ in liquid-phase CO_2 hydrogenation under relatively mild reaction conditions (total 4.0 MPa, 200 °C). *In situ* XAFS, *in situ* DRIFT spectroscopy and DFT calculations were employed to investigate the reaction mechanism. The experiments and comprehensive analyses revealed that abundant surface oxygen vacancies and the redox ability of Mo species in quasi-stable $\text{H}_x\text{MoO}_{3-y}$ endowed this catalyst with enhanced adsorption and activation capability to subsequently transform CO_2 to form the CO intermediate, and Pt NPs were found to act as H_2 dissociation sites to regenerate oxygen vacancies and as hydrogenation sites of CO intermediate to finally afford methanol. This study provides new insights into the design and development of high-performance heterogeneous catalysts for CO_2 hydrogenation reactions to produce methanol, which is a key chemical process for realizing CO_2 reduction and sustainable methanol production.

Experimental

Synthesis of oxide-supported Pt catalysts

The Pt catalyst supported on $\alpha\text{-MoO}_3$ (Pt/MoO_3) was prepared by a precipitation method using urea as a precipitant.⁴¹ $\alpha\text{-MoO}_3$ (1.0 g) was dispersed in 100 mL of distilled water containing 4.5 mL of K_2PtCl_4 solution (35 mM). To this suspension, 0.2 g of urea as a precipitation reagent was added, followed by vigorous stirring for 6 h at 95 °C to precipitate Pt^{2+} ions. The obtained slurry was centrifuged, washed with deionized water, and then dried at 100 °C in air overnight to give Pt/MoO_3 (unreduced sample). The catalyst used in the hydrogenation process was prepared by reduction of Pt/MoO_3 in a glass tube under a flow of H_2 (20 mL min^{-1}) for 30 min with a heating rate of 5 °C min^{-1} to give $\text{Pt}/\text{H}_x\text{MoO}_{3-y}(T)$ (T represents the reduction temperature (°C)). The Pt loading was determined to be 1.3 wt% by inductively coupled plasma (ICP) analysis. The $\text{Pt}/\text{H}_x\text{MoO}_{3-y}(T)$ catalysts with various Pt contents were prepared in the same manner using different amounts of K_2PtCl_4 solution.

Other oxide-supported Pt catalysts were prepared in the same manner described above except for using different oxides as supports. Pd, Re, Ru and Cu catalysts supported on MoO_3 were also prepared in the same manner described above except for using Na_2PdCl_4 , NH_4ReO_4 , $\text{RuCl}_3 \cdot n\text{H}_2\text{O}$, and $\text{Cu}(\text{NO}_3)_2 \cdot 3\text{H}_2\text{O}$ as the precursors, respectively, instead of K_2PtCl_4 .

Characterization

High-resolution transmission electron microscopy (HR-TEM) images were recorded on a JEOL ARM200F instrument operated at 200 kV accelerating voltage. The sample was dispersed in



ethanol by sonication, and the dispersion was dropped onto a Cu grid covered with carbon film in an Ar atmosphere to avoid sample oxidation. Power X-ray diffraction (XRD) patterns were obtained with a Rigaku Ultima IV diffractometer with Cu K_{α} radiation ($\lambda = 1.54056 \text{ \AA}$) operated at 40 kV and 40 mA. X-ray photoelectron spectroscopy (XPS) measurements were performed on a Shimadzu ESCA-3400 photoelectron spectrometer using Mg K_{α} radiation (1253.6 eV) X-ray source at $<10^{-5} \text{ Pa}$. Samples were introduced to the XPS analysis chamber without exposure to the air to avoid sample oxidation. All binding energies were calibrated with the adventitious carbon (C 1s) peak at 284.5 eV.

Mo K-edge and Pt L3-edge XAFS spectra were recorded at the BL01B1 beamline at the SPring-8 facility, Japan Synchrotron Radiation Research Institute (JASRI), Harima, Japan. Si(311) and Si(111) double-crystal monochromators were used for the Mo K-edge and Pt L3-edge XAFS measurements, respectively. For pseudo *in situ* XAFS measurement, the samples, pretreated in a flow of H_2 , were sealed in a polyethylene bags without exposure to the air, and subjected to the XAFS measurement at room temperature. For *in situ* Mo K-edge XAFS measurement, a pelletized unreduced Pt/MoO₃ sample ($\varphi 7 \text{ mm}$) was placed in a tailor-made quartz cell (Makuhari Rikagaku Garasu Inc.) equipped with a water-cooling condenser and an electric heater, which was connected to a gas-exchange system. After purging the cell with He, the sample was first reduced at 300 °C under a flow of 20% H_2/He (100 mL min⁻¹), kept at 200 °C, and then exposed to 20% CO_2/He (100 mL min⁻¹) and 20% H_2/He (100 mL min⁻¹) in turn. During these processes, Mo K-edge XAFS spectra were recorded in transmission mode to track the changes of Mo species. The obtained XAFS spectra were normalized by fitting the background absorption coefficient. After a k^3 -weighting, the extended XAFS (EXAFS) spectra were Fourier-transformed from the k space to the r space across the k range $3.0 < k (\text{\AA}^{-1}) < 11.0$ to obtain the radial distribution functions (RDFs).

Temperature programmed reduction with hydrogen (H_2 -TPR) was carried out using a BELCATII system (Microtrac-BEL Corp.) equipped with a thermal conductivity (TCD) detector. A sample (*ca.* 50 mg) mounted in a quartz vessel was pretreated in a flow of Ar (30 mL min⁻¹) at 150 °C for 60 min to remove the physisorbed water, and then cooled to 50 °C. TPR profiles were collected by heating the samples from 50 to 500 °C with a heating rate of 10 °C min⁻¹ under a flow of 5% H_2/Ar (50 mL min⁻¹). The effluent gas was passed through a trap containing a molecular sieve MS-4A to remove the produced water to determine the amount of H_2 consumed.

Thermogravimetric measurement (TG) was conducted in a flow of either air or N₂ to determine the amounts of hydrogen and oxygen vacancies introduced in molybdenum sub-oxide samples, respectively. The weight change curves were obtained on a Rigaku Thermo plus EVO II. Unreduced sample placed in an alumina pan was first reduced in a flow of H_2 (100 mL min⁻¹) at designated temperatures (100–400 °C) for 30 min, and then cooled to 50 °C. After switching the flow gas to either air or N₂ (100 mL min⁻¹), the temperature was increased from 50 to 450 °C at a heating rate of 10 °C min⁻¹. Based on the

weight changes observed under the two different conditions, the stoichiometric compositions of the samples were determined.

In situ DRIFT measurement

DRIFT spectra were measured using a Shimadzu IRSpirit spectrometer, equipped with a triglycine sulfate (TGS) detector at a resolution of 4 cm⁻¹. For *in situ* DRIFT measurement, unreduced sample was placed in an alumina pan, introduced into a stainless-steel heat chamber (S.T. Japan Inc.) equipped with a water-cooling system and connected to gas cylinders, and prerduced at 300 °C in a flow of H_2 (20 mL min⁻¹) for 30 min. After prerduction, the cell was kept at 250 °C and a background spectrum was obtained. Subsequently, 1.0 MPa of CO₂ and 1.0 MPa of H_2 were successively introduced into the *in situ* cell, and the DRIFT spectra were recorded every 30 min. Each DRIFT spectrum was obtained by subtracting the background spectrum from each measured spectrum.

General procedure for CO₂ hydrogenation

In a typical procedure, the as-prepared catalyst (*ca.* 50 mg) was placed in a glass tube, followed by reduction at 300 °C for 30 min in a flow of H_2 (20 min min⁻¹). The glass tube containing the prerduced catalyst (*ca.* 50 mg) and 1,4-dioxane (15 mL) were placed in a stainless-steel autoclave reactor (volume = 41 mL), purged three times with pure CO₂, and pressurized to 1.0 MPa with CO₂ and then to 4.0 MPa with H_2 (CO₂ : H_2 = 1 : 3). The reactor was heated to 200 °C and magnetically stirred (600 rpm) for 20 h. After the reaction, the reaction mixture was cooled to room temperature and depressurized, and the gas products were analyzed using a gas chromatograph (GC; Shimadzu GC-8A) with a 4 m active carbon column equipped with an FID detector and a methanizer (Shimadzu MTN-1). The liquid products were analyzed using GC-FID (column: Zebron ZB-FFAP, 50 m × 0.32 mm) using 1-butanol as an external standard. The TON values were determined by dividing the quantity of CO₂ converted by the number of moles of the total quantity of Pt contained in the catalyst. To examine the catalyst reusability, the catalyst was retrieved from the reaction solution by centrifugation (10 000 rpm, 5 min), washed with the solvent, and then subjected to next catalytic run.

DFT calculations

All DFT calculations were performed using the CASTEP program in Materials Studio 17.2. The Perdew–Burke–Ernzerhof exchange-correlation function within the generalized gradient approximation (GGA-PBE) with the ultrasoft core potential was employed for geometry optimization, and the double numerical plus *d*-function (DND) was chosen as the basis set. The electron configurations of the atoms were H: 1s¹, C: 2s²2p², O: 2s²2p⁴, Mo: 4s²4p⁶4d⁵5s¹, Pt: 5d⁹6s¹, the plane wave cutoff energy was set to 300 to 340 eV. Considering the layered structure of H_{0.9}MoO₃ in Pt/H_xMoO_{3-y}, a super cell slab model composed of H₃₂Mo₃₂O₉₆ including one Mo octahedra bilayer was constructed. The lattice parameters for the super cell are $b = 15.1776 \text{ \AA}$, $c = 15.4438 \text{ \AA}$, $\alpha = \gamma = 90^\circ$, $\beta = 93.727^\circ$. The *a*-axis



was taken as the direction of surface normal, and a was set to 30 Å including the vacuum region. For the slab model with a Pt NP, a Pt₂₀ cluster was loaded on the H_{0.9}MoO₃ (100) surface to model Pt/H_xMoO_{3-y} catalyst.^{42,43} The bottom MoO₆ layer was fixed at the corresponding bulk position, while the top MoO₆ layer, the Pt₂₀ cluster and the molecules in the gas phase were allowed to relax during geometry optimizations. The adsorption energy (E_{ads}) was defined as $E_{\text{ads}} = E_{\text{total}} - (E_{\text{sub}} + E_{\text{molecule}})$, where E_{total} , E_{sub} , and E_{molecule} are the total energies of the substrate optimized together with the adsorbate, the free substrate, and the free adsorbate molecule. The activation energy for transition state (TS) was defined as the difference energy between the TS and the local minimum just before the TS.

Results and discussion

Liquid-phase CO₂ hydrogenation over oxide-supported Pt catalysts

In a preliminary study, liquid-phase CO₂ hydrogenation was carried out using Pt NPs catalysts immobilized on various oxide supports (Pt content: *ca.* 3 wt%) to search for a catalyst that provides a high methanol yield. The CO₂ hydrogenation reaction was performed using a stainless autoclave reactor (volume = 41 mL) filled with 4.0 MPa of CO₂/H₂ gas (CO₂ : H₂ = 1 : 3) at 200 °C for 20 h using catalyst (50 mg) pretreated with H₂ at 300 °C for 30 min (Table 1 and Fig. 1a). The main products observed in this reaction were CO, methanol, and methane. High CO₂ conversion rates were attained when easily reducible oxides such as MoO₃, V₂O₅, Nb₂O₅ and WO₃ were used as supports; Pt/H_xMoO_{3-y} catalyst provided the highest CO₂

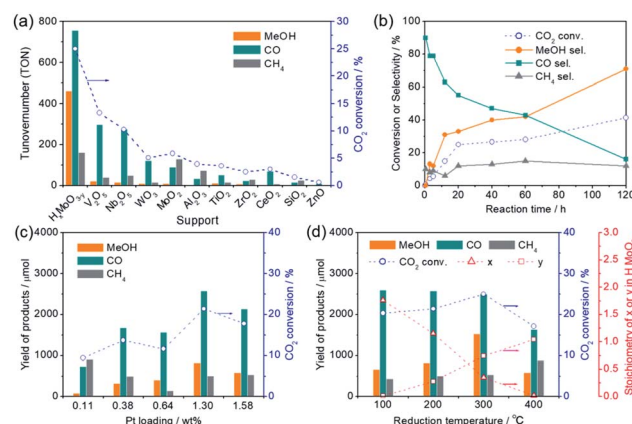


Fig. 1 (a) Comparison of catalytic performance of various oxide-supported Pt catalysts in the liquid-phase CO₂ hydrogenation reaction (catalysts were all reduced at 300 °C for 30 min in a flow of H₂). (b) Time course of the product selectivity and CO₂ conversion over Pt/H_xMoO_{3-y}(300) catalyst. (c) Effect of Pt loading on catalytic performance for Pt/H_xMoO_{3-y} catalyst (catalysts were all reduced at 200 °C for 30 min in a flow of H₂). (d) Effect of reduction temperature on catalytic performance for Pt/H_xMoO_{3-y}(T) catalyst and the stoichiometry of intercalated H atoms (x) and oxygen vacancies (y) in molybdenum sub-oxide (H_xMoO_{3-y}). Reaction conditions: catalyst (50 mg), 1,4-dioxane (15 mL), P_{CO₂} = 1.0 MPa, P_{H₂} = 3.0 MPa, 200 °C, 20 h.

conversion (25.0%) with the highest methanol selectivity (Sel_{MeOH} = 33%) among the catalysts examined, which corresponded to a 1.53 mmol yield of methanol after 20 h of reaction (methanol production rate = 1.53 mmol g_{cat}⁻¹ h⁻¹) (entry 1), while Pt/V₂O₅, Pt/Nb₂O₅ and Pt/VO₂ catalysts gave CO as the main product and methanol was hardly produced (Sel_{MeOH} = 5–

Table 1 Liquid-phase CO₂ hydrogenation using various oxide-supported Pt catalysts^a

Entry	Catalyst	Metal loading ^b [wt%]	CO ₂ conv. [%]	Selectivity [%]			Total TON ^c	TON for MeOH ^c
				MeOH	CO	CH ₄		
1	Pt/H _x MoO _{3-y}	1.3	25.0	33	55	12	1379	462
2	Pt/V ₂ O ₅	2.6	13.3	6	83	11	360	22
3	Pt/Nb ₂ O ₅	2.2	10.3	5	81	14	340	16
4	Pt/VO ₂	2.5	5.1	7	82	11	148	10
5	Pt/MoO ₂	1.8	5.9	4	39	57	231	10
6	Pt/γ-Al ₂ O ₃	2.6	3.9	0	31	69	107	0
7	Pt/TiO ₂	3.2	3.6	15	66	19	79	12
8	Pt/ZrO ₂	2.7	2.5	12	39	49	62	8
9	Pt/CeO ₂	2.7	3.0	4	86	10	81	3
10	Pt/SiO ₂	2.6	1.5	0	39	61	42	0
11	Pt/ZnO	2.8	0.6	20	75	5	14	3
12	Pd/MoO ₃	3.0 ^f	3.2	6	56	38	41	3
13	Re/MoO ₃	3.0 ^f	2.3	5	23	72	51	3
14	Ru/MoO ₃	3.0 ^f	0.9	37	50	13	12	4
15	Cu/MoO ₃ ^d	3.0 ^f	1.5	0	5	95	11	0
16	Cu/ZnO ^d	30.0 ^f	0.4	19	12	69	9	0.3
17	H _x MoO _{3-y} ^e	—	3.0	0	8	92	—	—
18	MoO ₃	—	0.3	0	21	79	—	—

^a Reaction conditions: catalyst (50 mg), 1,4-dioxane (15 mL), P_{CO₂} = 1.0 MPa, P_{H₂} = 3.0 MPa, 200 °C, 20 h. Catalysts were reduced at 300 °C for 30 min in a flow of H₂. ^b Determined by ICP analysis. ^c TON was calculated on the basis of total active metals contained in the catalysts. ^d Prepared by the wet impregnation method. ^e Synthesized by a solvothermal method according to ref. 44. ^f Nominal content.



7%) (entries 2–4). For the $\text{Pt}/\text{H}_x\text{MoO}_{3-y}$ catalyst, the turnover number (TON) calculated for CO_2 conversion, based on the number of Pt atoms contained in the catalyst, was 1379, and the TON for methanol production was 462, demonstrating that the CO_2 hydrogenation reaction occurs in a catalytic manner. Interestingly, Pt supported on MoO_2 exhibited a lower CO_2 conversion (5.9%) and a lower methanol selectivity ($\text{Sel}_{\text{MeOH}} = 4\%$) compared with $\text{Pt}/\text{H}_x\text{MoO}_{3-y}$ under the same conditions (entry 5). Pt catalysts supported on amphoteric oxides, such as Al_2O_3 , TiO_2 , ZrO_2 , and CeO_2 , exhibited low CO_2 conversions (entries 6–9) and low methanol selectivities. As the mono-component counterparts, pristine MoO_3 (entry 18), defective $\text{H}_x\text{MoO}_{3-y}$ (prepared by a solvothermal method)⁴⁴ (entry 17) and Pt/SiO_2 catalyst (entry 10) were also examined; however, the CO_2 conversions (0.3%, 3.0% and 1.5%, respectively) over these catalysts in 20 h were far below that of the $\text{Pt}/\text{H}_x\text{MoO}_{3-y}$ catalyst and the formation of methanol was not observed. It was thus clarified that the nature of the oxide support has a dramatic effect on the catalytic performance of the Pt catalyst in liquid-phase CO_2 hydrogenation. In addition, Pd, Re, Ru, and Cu catalysts supported on MoO_3 (entries 12–15), which were prepared by a similar method (see Experimental section), and Cu/ZnO catalyst (entry 16; nominal Cu content = 30.0 wt%) traditionally used for gas-phase CO_2 hydrogenation reaction showed low catalytic activities and low methanol yields under the conditions adopted in this study. The significantly low catalytic activity observed for the benchmark Cu/ZnO catalyst may be attributed to the use of organic solvent which is unmatched for Cu-based catalyst and a relatively lower operation temperature than that usually employed for Cu-based catalysts. These results indicate that Pt is an indispensable component in the catalytic reaction, and the synergistic effect between Pt and Mo sub-oxide plays a critical role in achieving a high catalytic performance.

Liquid-phase CO_2 hydrogenation over molybdenum oxide-supported Pt catalyst

Fig. 1b shows the time variation of product yields during the reaction on the $\text{Pt}/\text{H}_x\text{MoO}_{3-y}$ (300) at 200 °C. CO was rapidly produced as the main product in the initial stage of the reaction

and yields of methanol and methane steadily increased over time along with a gradual decrease in the yield of CO. The conversion of CO_2 and the selectivity for methanol obtained at 200 °C after 120 h of reaction reached 41.4% and 71%, respectively, which corresponded to a 5.38 mmol yield of methanol (methanol production rate = 0.896 mmol g_{cat}⁻¹ h⁻¹). The decreased conversion rate of CO_2 in the latter stage of reaction may reflect the gradual reduction of CO_2/H_2 gas pressures inside the reactor. In methanol synthesis from CO_2 and H_2 , (i) the CO formation route and (ii) the HCOO^- (formate) formation route are known to be major reaction pathways.^{6,45,46} Considering the product distribution and the fact that formate was not detected by liquid chromatography in the reaction solution, methanol is likely to be produced *via* the formation of CO as an intermediate (*i.e.* RWGS reaction), while a small fraction of CO is transformed irreversibly to methane.

Fig. 1c shows the effect of the loading amount of Pt on the catalytic activity. The highest yield and selectivity for methanol formation was achieved when the Pt loading was 1.3 wt%. Although the conversion of CO_2 and the yield of methanol tended to increase with increasing Pt loading, they decreased when the Pt loading exceeded 1.5 wt%. Pt L3-edge XAFS analysis (Fig. S1 in ESI†) and Pt 4f XPS spectra (Fig. S2 in ESI†) verified that the Pt species on these catalysts exist as metallic Pt(0) NPs in all cases and the size of the Pt NPs increases with increasing Pt content. The catalytic activity was not directly proportional to the mean surface area of surface-exposed Pt atoms determined by CO pulse measurement (Fig. S3 in ESI†), suggesting that the CO_2 hydrogenation is catalyzed not solely on the Pt NPs surface, but at the interface between the Pt NPs and the $\text{H}_x\text{MoO}_{3-y}$ support, and that larger Pt NPs are unfavorable due to a decrease in the number of Pt– $\text{H}_x\text{MoO}_{3-y}$ interfacial sites.

Over the $\text{Pt}/\text{H}_x\text{MoO}_{3-y}$ (300) catalyst, almost no product was detected in the absence of CO_2 (trace of CH_4 may be from carbonaceous species contained in the catalyst) (Table 2, entry 2). In fact, in an isotopic experiment using ¹³ CO_2 as a reaction gas instead of ¹² CO_2 , a signal at $m/z = 33$ assigned to ¹³ CH_3OH was detected (Fig. S4 in ESI†), confirming that CO_2 is the sole carbon source for CO, methanol and methane. More noteworthy is the fact that a substantial amount of CO was produced even in the absence of H_2 (entry 3). Considering that such a huge CO

Table 2 Methanol production *via* CO_2 hydrogenation using $\text{Pt}/\text{H}_x\text{MoO}_{3-y}$ (300) catalyst under different conditions^a

Entry	Conditions	CO_2 conv. [%]	Yield [μmol]				Total TON ^b
			MeOH	CO	CH_4		
1	$P_{\text{CO}_2} = 1.0 \text{ MPa}$ $P_{\text{H}_2} = 3.0 \text{ MPa}$	25.0	1526	2501	532	1379	
2	No CO_2 $P_{\text{H}_2} = 3.0 \text{ MPa}$	0	0	<1	66	—	
3	$P_{\text{H}_2} = 1.0 \text{ MPa}$ No H_2	10.9	0	1541	443	600	
4	$P_{\text{CO}_2} = 0.1 \text{ MPa}$ $P_{\text{H}_2} = 3.0 \text{ MPa}$	(CO conv.) 57.8	371	—	684	310	

^a Reaction conditions: catalyst ($\text{Pt}/\text{H}_x\text{MoO}_{3-y}$ (300), 50 mg), 1,4-dioxane (15 mL), 200 °C, 20 h. ^b TON was calculated on the basis of total Pt atoms contained in the catalyst.



evolution was not observed on most of the other supported Pt catalysts (Fig. S5 in ESI†), the oxygen vacancies created on $H_x\text{MoO}_{3-y}$ possibly functioned as deoxygenation sites to reduce CO_2 to CO . Furthermore, introduction of CO (0.1 MPa) instead of CO_2 resulted in the formation of substantial amounts of methanol and methane at 200 °C (entry 4), again confirming that methanol as well as methane are produced *via* hydrogenation of CO as an intermediate over the $\text{Pt}/H_x\text{MoO}_{3-y}(300)$ catalyst.

Structural analysis of Pt-loaded molybdenum oxide

The HR-TEM image of the $\text{Pt}/H_x\text{MoO}_{3-y}(300)$ catalyst revealed that the Pt NPs with an average particle size of 2.4 nm are uniformly immobilized on the Mo oxide particles (Fig. 2a).

In the enlarged HR-TEM image, the interplanar distance of the Pt NPs was *ca.* 1.95 Å, matching well the (200) plane of fcc Pt (Fig. 2b). The lattice fringes seen in the Mo oxide particle were not clear, being considerably disconnected or distorted in most cases (Fig. 2c). Only a few diffraction spots were observable in the selected electron diffraction (SAED) pattern (inset in Fig. 2c), indicating a short-range order atomic arrangement, which may be because of the introduction of many defect sites. Meanwhile,

some clear lattice fringes were partly observed in some Mo oxide particles (Fig. 2d), which are consistent with the *d*-spacing of the (001) and (010) planes of the monoclinic $H_{0.9}\text{MoO}_3$ phase.^{47–49} The corresponding SAED pattern exhibited clear spots assignable to the (001) and (010) planes (inset in Fig. 2d). Two interplanar spacings were found to be 0.41 and 0.37 nm with a separation angle of 91–92°, which matched well with the monoclinic structure of the $H_{0.9}\text{MoO}_3$ phase with the $P2_1/c$ space group as shown in Fig. 2e, confirming the existence of crystalline $H_{0.9}\text{MoO}_3$ phases in the short-range order.

Interestingly, the catalytic activity of the $\text{Pt}/H_x\text{MoO}_{3-y}$ catalyst varied with the temperature of H_2 reduction (Fig. 1d); both the CO_2 conversion and the yield of methanol tended to increase with increasing reduction temperature. In particular, the highest CO_2 conversion (25%) and methanol selectivity (33%) were attained when the catalyst was reduced at 300 °C. However, a marked drop of catalytic performance (conv. = 17.1%, $\text{Sel}_{\text{MeOH}} = 19\%$) was observed for reduction at 400 °C. $\text{H}_2\text{-TPR}$ is commonly used to help understand the reduction behavior of metal oxides. Fig. 3a compares the $\text{H}_2\text{-TPR}$ profiles of the as-synthesized oxide-supported Pt catalysts. The as-prepared Pt/MoO_3 sample gave an intense reduction peak at 136 °C, while such a large H_2 consumption was not observed for the other oxide-supported Pt catalysts. The amount of H_2 consumed below 200 °C was calculated to be 4.95 mmol- H_2 per g-catalyst. The molar ratio of H atoms consumed per mole of Pt atoms contained in the catalyst (H/Pt) was 149 and that used per mole number of Mo atoms (H/Mo) was 1.44, whereas the as-prepared Pt/SiO_2 showed a quite low consumption of H_2 (H/Pt molar ratio of 2.2). This result indicates that the large H_2 consumption on Pt/MoO_3 at around 136 °C is not only due to the reduction of the Pt precursor but is attributed to the reduction of the MoO_3 support. An additional H_2 consumption at around 280 °C may be associated with the formation of oxygen vacancies, as will be discussed later. Importantly, pristine MoO_3 exhibited no H_2 consumption below 500 °C, indicating that Pt assists in the reduction of the MoO_3 support by facilitating the dissociation of molecular H_2 (namely, the H-spillover process). Such a high reactivity of intracrystalline oxygen atoms in MoO_3 may well be responsible for the high CO_2 hydrogenation performance.

To track the crystallographic changes occurring with H_2 reduction at the different temperatures, XRD measurements were performed (Fig. 3b). The diffraction patterns of $\text{Pt}/H_x\text{MoO}_{3-y}(100)$ were assigned to orthorhombic $\alpha\text{-MoO}_3$ (PDF #5-0508) and monoclinic $H_{0.9}\text{MoO}_3$ (PDF #53-1024), while the peaks of unreduced Pt/MoO_3 were all indexed to orthorhombic $\alpha\text{-MoO}_3$. $\text{Pt}/H_x\text{MoO}_{3-y}(200)$ showed dominant peaks assigned to $H_{0.9}\text{MoO}_3$ with decreased diffraction intensities, and $\text{Pt}/H_x\text{MoO}_{3-y}(300)$ exhibited almost no distinct diffractions, indicating a collapse of the $H_{0.9}\text{MoO}_3$ phase and a disordered atomic arrangement (the $H_{0.9}\text{MoO}_3$ phase may partly exist, as observed by HR-TEM). The orthorhombic $\alpha\text{-MoO}_3$ used as a support in this study is composed of edge-sharing MoO_6 octahedra bilayers stacked along with [010] due to van der Waals interaction.^{50,51} As demonstrated in many previous studies, H-spillover occurs on noble metal catalysts supported

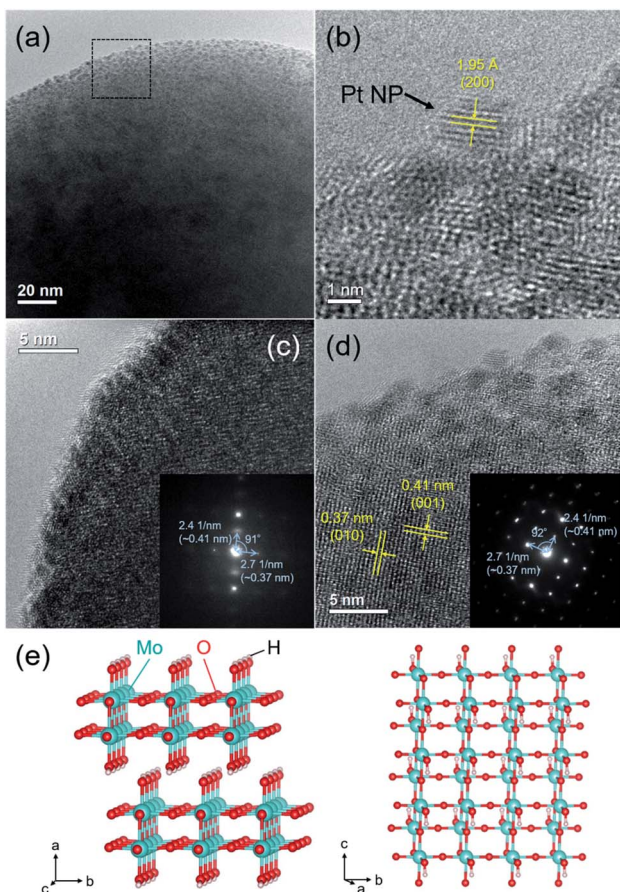


Fig. 2 (a) HR-TEM image, (b–d) magnified HR-TEM images (inset shows the corresponding SAED patterns of the $\text{Pt}/H_x\text{MoO}_{3-y}(300)$ catalyst, and (e) illustrations of the monoclinic $H_{0.9}\text{MoO}_3$ crystal structure.



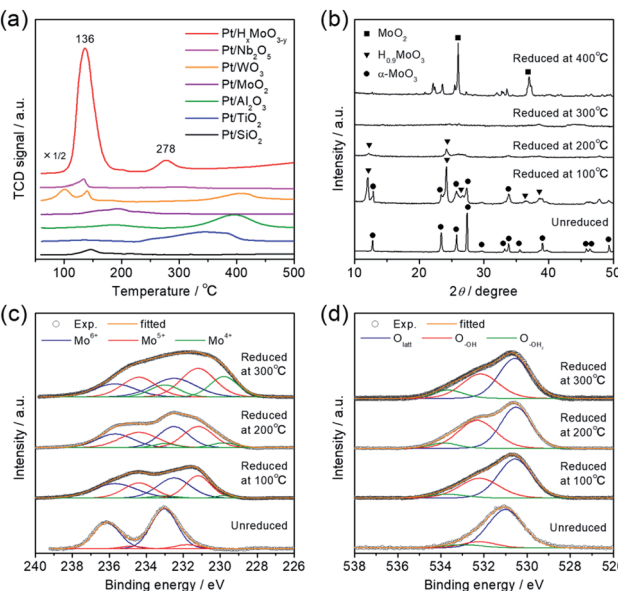
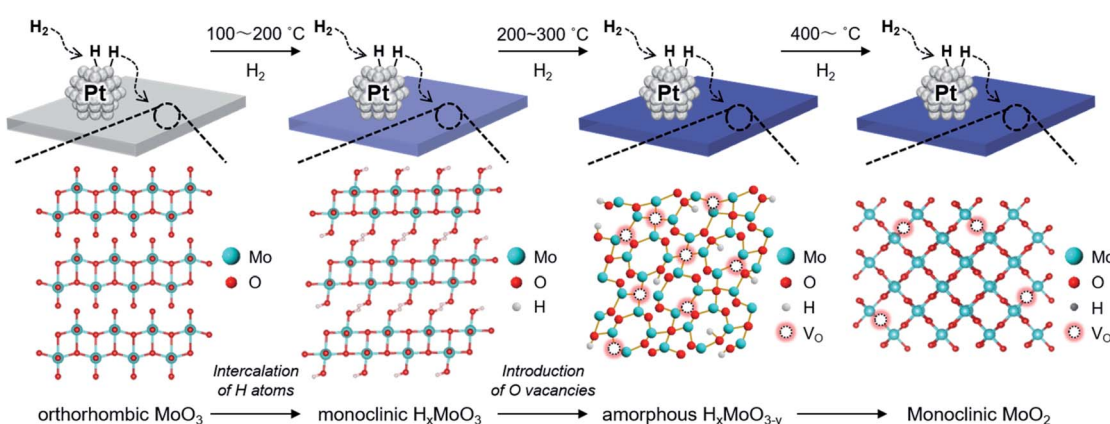


Fig. 3 (a) H₂-TPR profiles of Pt catalysts supported on various metal oxides. (b) XRD patterns, (c) Mo 3d XPS spectra, and (d) O 1s XPS spectra of un-reduced Pt/MoO₃ and Pt/H_xMoO_{3-y} catalysts reduced with H₂ at different temperatures.

on reducible metal oxides in the presence of H₂, in which molecular H₂ is dissociated over the noble metal NPs surface (H₂ → 2H⁺ + 2e⁻) and thus protons (H⁺) and free electrons are concurrently injected into the metal oxide matrices.^{52,53} In the case of the combination of the Pt NPs and α-MoO₃, H₂ dissociation occurs on the Pt NPs at around 140 °C (as shown in the H₂-TPR, see Fig. 3a), and the dissociated H⁺ atoms are coordinated to the interlayer terminal oxygen atoms to form hydroxyl groups, which yields a class of H_xMoO₃ materials (0 < x < 2), namely, hydrogen molybdenum bronze,^{47–49} as depicted in the schematic of Scheme 1. During this H-spillover process, the free electrons are trapped by Mo⁶⁺ ions (Mo⁶⁺ + e⁻/2e⁻ → Mo⁵⁺/Mo⁴⁺), and thus a great number of low-valence Mo species are generated. The relevant intercalation chemistry on α-MoO₃ is already well established by earlier studies.^{41–43,54–57} A further

temperature increase to 200–300 °C causes dehydration of H_xMoO₃ (as shown in the H₂-TPR, see Fig. 3a), in which lattice oxygen atoms (mainly bi-bridging oxygen atoms) are easily expelled by the H⁺ ions (2H⁺ + 2e⁻ + O₂ → V_O + H₂O),^{58,59} thus resulting in a further greater reduction of H_xMoO₃ to the quasi-stable H_xMoO_{3-y} sub-oxide which has abundant oxygen vacancies. Introduction of massive amounts of oxygen vacancies causes order-disorder transitions in the metal oxide (as illustrated in Scheme 1), which accounts for the significantly decreased diffraction intensities for Pt/H_xMoO_{3-y}(200) and Pt/H_xMoO_{3-y}(300). As previously reported, the intercalation of H atoms and the introduction of oxygen vacancies into the MoO₃ matrix increases the electron density of the entire oxide particle, fills the 4d Mo level, and brings about new energy levels near the conduction band (CB), which consequently leads to the emergence of new absorption bands due to surface plasmon resonance (SPR).^{41,60–62} This was corroborated by UV-vis-NIR measurement (Fig. S6 in ESI†), in which a strong absorption across the visible to NIR region with an intense SPR peak was observed for the reduced samples, while a limited absorption in the UV region was observed for the un-reduced Pt/MoO₃ sample. Further increase in the reduction temperature to 400 °C led to the transition to the MoO₂ phase, which has a distorted monoclinic rutile structure.

The intercalation of H atoms and the formation of oxygen vacancies within the Mo oxide matrices upon H₂ reduction was corroborated by XPS measurement. From the Mo 3d XPS spectrum (Fig. 3c), it was confirmed that low-valence Mo species (Mo⁵⁺/Mo⁴⁺) were formed after H₂ reduction, while Mo⁶⁺ species mainly existed before reduction. The concentrations of these low-valence Mo species increased with rise in the reduction temperature. The proportion of these low-valence Mo species was determined as: Mo⁵⁺ 42.7%, Mo⁴⁺ 3.8% (100 °C reduction) → Mo⁵⁺ 47.6%, Mo⁴⁺ 8.2% (200 °C reduction) → Mo⁵⁺ 42.0%, Mo⁴⁺ 23.7% (reduction at 300 °C), suggesting that generation of Mo⁴⁺ mainly results from the formation of an oxygen vacancy.⁶³ A similar reduction behavior for Mo species and the introduction of oxygen vacancies were corroborated by inspection of the Mo K-edge X-ray absorption near edge structure (XANES) spectra and the Fourier transforms of extended XAFS (EXAFS)

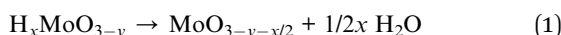


Scheme 1 Schematic illustration of the crystallographic changes of Pt/H_xMoO_{3-y} upon H₂ reduction.



spectra, respectively (see Fig. S7 in ESI; † see also Fig. 5). In the O 1s XPS spectra (Fig. 3d), un-reduced Pt/MoO₃ exhibited two main peaks which are ascribed to lattice oxygen (O_{latt}; 530.5 eV) and surface hydroxyl groups (O_{–OH}; 532.3 eV). Note that the samples were introduced to the XPS analysis chamber without exposure to the air, thereby excluding the possibility of adsorbed oxygen species. For the series of Pt/H_xMoO_{3–y} samples, the peak for the O_{–OH} species increased in intensity, and additional tailings, assigned to the formation of OH₂ groups weakly coordinated to Mo atoms (O_{–OH₂}), were observed at the higher binding energy region at about 533.6 eV. The proportion of these hydroxyl species ((O_{–OH} + O_{–OH₂})/O_{total}) was found to increase significantly upon H₂ reduction (un-reduced Pt/MoO₃ (20.3%) → Pt/H_xMoO_{3–y} (41–49%)), evidencing the H⁺-intercalation upon H₂ reduction process.⁶⁴

The above results verify the co-existence of the intercalated H atoms and oxygen vacancies in Pt/H_xMoO_{3–y}, which accompanies the formation of low-valence Mo species. To quantify the amounts of doped H atoms and oxygen vacancies, TG analysis was performed.^{65,66} Upon heat treatment of oxygen-defective H_xMoO_{3–y} in an inert gas flow, a dehydration reaction may occur through eqn (1):



However, upon heat treatment in an air gas flow, both the dehydration reaction and a filling of the oxygen vacancies to form molybdenum trioxide (MoO₃) possibly occur through eqn (2):



Therefore, the stoichiometry of the doped H atoms (x) and the oxygen vacancies (y) in H_xMoO_{3–y} can be calculated from the changes in thermal weight observed under the two different conditions (Fig. S8 in ESI†). Assuming the composition of the oxygen-defective molybdenum oxide of H_xMoO_{3–y}, the composition was determined as H_{1.76}MoO_{2.99} (100 °C reduction) → H_{1.15}MoO_{2.72} (200 °C reduction) → H_{0.35}MoO_{2.26} (300 °C reduction) from the results of TG analysis, showing that the intercalated H atoms are continuously removed *via* thermal dehydration, while an increased number of oxygen vacancies is introduced after H₂ reduction at elevated temperatures. As shown in Fig. 1d, the CO₂ conversion and the yield of methanol increased along with an increase in the stoichiometry of the oxygen vacancy (y) in the Pt/H_xMoO_{3–y}(T) catalysts in the reduction temperature range of 100 to 300 °C. It should be mentioned that the stoichiometry of x and y in the Pt/H_xMoO_{3–y}(400) catalyst was almost equal to 0.0 and 1.0, respectively, indicating the formation of MoO₂, which is consistent with XRD data (Fig. 3b). The decreased activity for Pt/H_xMoO_{3–y}(400) is probably attributed to the transition to monoclinic MoO₂ with less oxygen vacancies. These results indicate the possibility that the oxygen vacancies formed in the quasi-stable H_xMoO_{3–y} sub-oxide during H₂ reduction play a pivotal role in the CO₂ hydrogenation and in the production of methanol.

Understanding the role of the oxygen vacancy

CO₂ adsorption is generally regarded as being a prerequisite in the CO₂ reduction process. Based on the above experiments, it may be hypothesized that the presence of abundant surface oxygen vacancies endows the Pt/H_xMoO_{3–y} with enhanced CO₂ adsorption, leading to an efficient activation of CO₂ on the surface. This was verified by the CO₂ adsorption measurement (Fig. S9 in ESI†). The Pt/H_xMoO_{3–y}(300), which possessed the highest oxygen vacancy concentration, showed a much higher CO₂ adsorption capacity than the un-reduced Pt/MoO₃.

To understand the role of the oxygen vacancy at an atomic level, the CO₂ adsorption energies over the surface of oxygen-defective and perfect molybdenum oxide were calculated using density function theory (DFT) calculations. Considering the layered structure of H_{0.9}MoO₃ in the Pt/H_xMoO_{3–y} catalyst, the (100) surface of H_{0.9}MoO₃ was chosen to construct the slab model. For oxygen-defective slab model, oxygen vacancy was created at the bi-bridging oxygen atom position.^{58,59} The adsorption energy of CO₂ on the oxygen-defective H₃₀Mo₃₂O₉₅ surface was calculated to be $-8.3 \text{ kcal mol}^{-1}$, which was significantly higher than that on the perfect H₃₀Mo₃₂O₉₆ surface ($-0.23 \text{ kcal mol}^{-1}$), indicating that an oxygen defect site is favorable for adsorption of CO₂.^{67,68} When CO₂ is adsorbed at the oxygen vacancy site, the CO₂ molecule becomes bent, and the O–C–O angle changes from 179.2° to 125.1°, and the C–O bond length is extended from 1.178 Å to 1.224/1.370 Å (Fig. 4a), while those adsorbed on the perfect surface were unchanged (Fig. 4b).⁶⁸ These findings indicate that the C–O bonds are weakened on the oxygen-defective H₃₀Mo₃₂O₉₅ surface. Furthermore, Mulliken population analysis demonstrated that the total charge (Δq) of CO₂ is increased from +0.0e (on perfect H₃₀Mo₃₂O₉₆) to $-0.47e$ (on oxygen-defective H₃₀Mo₃₂O₉₅).⁶⁸ The CO₂ molecule adsorbed on an oxygen vacancy gains more electrons from the low-valence Mo ions (*i.e.* Mo⁵⁺/Mo⁴⁺ species) with partially higher electron densities, which leads to polarization of CO₂, which, therefore, promotes the activation and dissociation of the CO₂ molecule.

To understand the catalytic role of the oxygen vacancy in CO₂ hydrogenation, *in situ* XAFS measurement was performed.

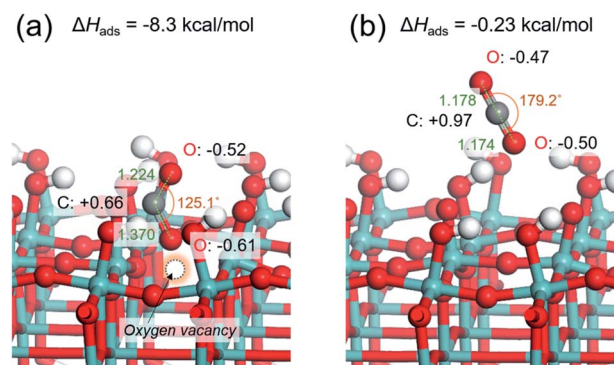


Fig. 4 Optimized structure models for CO₂ adsorbed on (a) oxygen-defective H_xMoO_{3–y} (H₃₀Mo₃₂O₉₅) surface and (b) perfect H_xMoO₃ (H₃₀Mo₃₂O₉₆) surface.

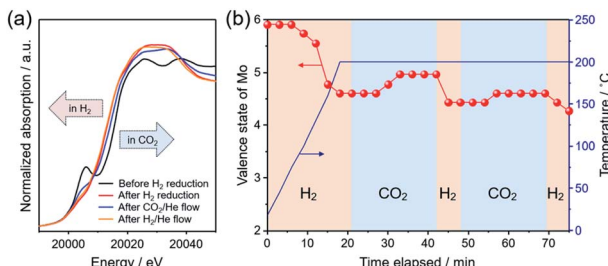


Fig. 5 (a) *In situ* Mo K-edge XANES spectra of Pt/MoO₃ measured at 200 °C; before H₂ reduction (black line), after H₂ reduction under a flow of 20% H₂/He (red line), after subsequent flow of 20% CO₂/He (blue line) and subsequent flow of 20% H₂/He (orange line). (b) Change of valence state of the Mo species during the *in situ* XAFS measurement. The valence state was determined by a linear interpolation method.

Fig. 5a shows the XANES spectra in the Mo K-edge region for the as-prepared Pt/MoO₃ sample before and after H₂ reduction at 200 °C, and for those measured after subsequent exposure to H₂ and CO₂ at 200 °C. The as-prepared Pt/MoO₃ sample exhibited an absorption spectrum with a characteristic pre-edge absorption at 20 006 eV, which was almost the same as that of orthorhombic α -MoO₃. After H₂ reduction at 200 °C, the pre-edge absorption was significantly diminished and the absorption edge position clearly shifted towards the lower energy region, which led to an absorption spectrum close to that of monoclinic MoO₂. This is because of the phase transition from the orthorhombic α -MoO₃ with a distorted octahedral geometry to the H_xMoO_{3-y} sub-oxide with a symmetric octahedral geometry and low-valence Mo atoms.^{69,70} Such a spectral change upon H₂ reduction is consistent with the results of XRD and Mo 3d XPS. After the introduction of the 20% CO₂/He flow gas at 200 °C, the absorption edge shifted slightly towards the higher energy region, showing substantial oxidation of Mo species with CO₂. The subsequent switching to 20% H₂/He flow caused an absorption edge shift back towards the lower energy region, indicating a re-reduction of Mo species with H₂. The average valence state of Mo ions in the catalyst during the *in situ* XAFS measurement was determined from the absorption edge position (E_0) using a linear interpolation method and was plotted as a function of time. As shown in Fig. 5b, the average valence state of Mo increased/decreased reversibly for the CO₂/H₂ flow at 200 °C, clearly demonstrating that a redox event involving the Mo species took place during reduction of CO₂. The molybdenum oxide is initially reduced by H atoms dissociated on Pt NPs through a H-spillover process to produce oxygen vacancies. The CO₂ molecule is adsorbed and activated at the oxygen vacancy interbedded between the under-coordinated Mo (Mo⁵⁺/Mo⁴⁺) sites, which leads to the formation of CO and a concurrent replenishment of the oxygen vacancy (CO₂ + V_O → CO + O_O) accompanied by the oxidation of Mo atoms. This was also corroborated by Mo 3d XPS spectra, in which the proportion of Mo⁴⁺ species considerably decreased and the average oxidation number of Mo increased upon a treatment with 1.0 MPa CO₂ at 200 °C (Fig. S10 in ESI[†]). In the presence of H₂, the oxygen

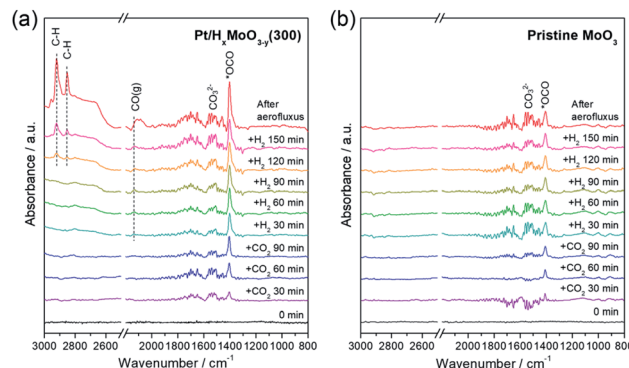


Fig. 6 *In situ* differential DRIFT spectra of adsorbed species on (a) Pt/H_xMoO_{3-y}(300) catalyst and (b) pristine MoO₃.

vacancy can be regenerated by the reaction with H atoms, thus the catalytic cycle can be achieved. This process can be understood as an oxygen-vacancy-mediated “reverse Mars–van Krevelen (M–vK)⁷¹” mechanism.^{31,33,41,72} Thus, DFT calculations and *in situ* XAFS measurement revealed that the oxygen vacancy sites in oxygen-defective H_xMoO_{3-y} not only stabilize CO₂ by donating electrons, but also promote dissociation of CO₂ through electron transfer from the abundant localized electrons on the ionic Mo (Mo⁵⁺/Mo⁴⁺) species to CO₂, which should be effective for promoting the cleavage of CO₂ and the subsequent hydrogenation reactions.

The CO₂ hydrogenation mechanism

To monitor the CO₂ hydrogenation process, *in situ* DRIFT experiments were performed (Fig. 6). Prior to DRIFT spectra measurement, the as-synthesized Pt/MoO₃ sample was pretreated under H₂ flow for 30 min at 300 °C to yield Pt/H_xMoO_{3-y}(300), followed by cooling to 250 °C, and then 1.0 MPa of CO₂ and 2.0 MPa of H₂ were successively introduced.

After the introduction of CO₂, two distinct peaks were observed at 1404 and at around 1530 cm⁻¹, the former being commonly assigned to symmetric stretching vibration mode of monodentate carbonate species ($\nu_s(\text{OCO}^-)$) (major species) and the latter being characteristic of the C=O stretching vibration of bidentate carbonates (minor species).^{23,73–75} After the introduction of H₂, a broad band assignable to gaseous CO was observed at around 2130 cm⁻¹,^{74,76} indicating that the CO₂ adsorbed on the catalyst underwent deoxygenation to produce CO, although such a peak was not observed before H₂ introduction because of only a small yield of CO. Along with the increase in time, several additional features associated with the hydrogenated products were observed with increased IR intensity; the peaks observed at 2851 and 2922 cm⁻¹ are assignable to stretching vibrations of C–H bond.^{76,77} The tailing band observed at around 1300–1400 cm⁻¹ is assignable to hydroxyl O–H deformation vibration and CH₃ deformation vibration. The emergence of these bands indicate the formation of methanol over the Pt/H_xMoO_{3-y}(300) catalyst *via* hydrogenation of activated CO₂ intermediates or gaseous CO. IR bands associated with formate intermediates were not detected by *in situ* DRIFT

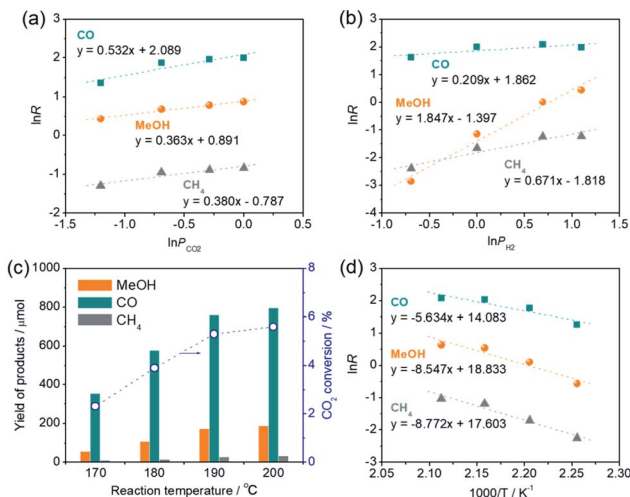


Fig. 7 (a) Double logarithm plots of reaction rate (R) and the partial pressure of CO_2 (P_{CO_2}), (b) double logarithm plots of reaction rate (R) and the partial pressure of H_2 (P_{H_2}), (c) effect of reaction temperature on catalytic performance, and (d) Arrhenius plots for the $\text{Pt}/\text{H}_x\text{MoO}_{3-y}(300)$ catalyst. Reaction conditions: catalyst (50 mg), 1,4-dioxane (15 mL), reaction time = 2 h.

analysis, again elucidating that hydrogenation of CO_2 on $\text{Pt}/\text{H}_x\text{MoO}_{3-y}$ catalyst occurs *via* the “RWGS-CO pathway”. It is also noteworthy that CO/methanol were produced even in the absence of solvent, demonstrating the availability of $\text{Pt}/\text{H}_x\text{MoO}_{3-y}$ catalyst in gas-phase CO_2 hydrogenation reaction to produce CO/methanol. In contrast, the intensity of the IR band for CO_2 adsorbed on pristine MoO_3 was apparently less than that adsorbed on $\text{Pt}/\text{H}_x\text{MoO}_{3-y}(300)$, indicating a much larger amount of adsorption sites for CO_2 exists on $\text{Pt}/\text{H}_x\text{MoO}_{3-y}(300)$. Furthermore, the IR bands associated with the hydrogenated carbon products were scarcely observed on pristine MoO_3 , demonstrating the role of Pt NPs as a hydrogenation center.

The reaction rate (R) of CO_2 hydrogenation can be expressed by $R = k \times P_{\text{CO}_2}^\alpha \times P_{\text{H}_2}^\beta$, where k is the rate constant, P_{CO_2} and

P_{H_2} represent the partial pressure of CO_2 and H_2 , and α and β represent the reaction order of CO_2 and H_2 , respectively. Kinetic analyses demonstrated that the reaction order of CO_2 (α) for CO production (0.532) was apparently larger than those for methanol production (0.363) and CH_4 production (0.380), indicating that the CO formation step is primarily governed by the CO_2 pressure and H_2 is rarely involved in this step. However, the reaction orders of H_2 (β) for methanol production (1.847) and CH_4 production (0.671) were much larger than that for CO production (0.209), indicating that methanol and CH_4 are produced from a CO intermediate *via* hydrogenation and the methanol production rate is strongly dependent on the H_2 pressure. These results are consistent with the conclusions drawn by catalytic experiments and the *in situ* DRIFT spectra measurement whereby CO is produced *via* deoxygenation of CO_2 at the oxygen vacancy sites and methanol and CH_4 are produced *via* hydrogenation of the CO on the Pt NPs. Furthermore, the reaction order of H_2 (β) for methanol production (1.847) was close to 2, which is consistent with the stoichiometric ratio of the CO hydrogenation reaction to produce methanol ($\text{CO} + 2\text{H}_2 \rightarrow \text{CH}_3\text{OH}$). Reaction rates decreased as the reaction temperature was lowered (Fig. 7c), although methanol synthesis from CO_2/H_2 favors lower reaction temperature due to an exothermic reaction. This is probably because of the RWGS reaction, an endothermic process ($\text{CO}_2 + \text{H}_2 \rightarrow \text{CO} + \text{H}_2\text{O}; \Delta H_{298}^0 = 41.2 \text{ kJ mol}^{-1}$), dominantly takes place in the early stage of reaction. From the Arrhenius plots, the activation energies for the production of CO, methanol, and CH_4 were determined as 46.8, 71.1, and 72.9 kJ mol^{-1} , respectively (Fig. 7d), verifying that the former deoxygenation reaction of CO_2 to produce CO is energetically more favorable than the latter hydrogenation reactions of the CO intermediate.

To draw a possible reaction pathway for CO_2 hydrogenation whereby methanol is produced over the $\text{Pt}/\text{H}_x\text{MoO}_{3-y}$ catalyst, DFT calculations using the periodic slab model were performed. Based on the HR-TEM observation results and previous literature,^{42,43} a slab model composed of a Pt_{20} cluster immobilized on the (100) exposed surface of $\text{H}_{30}\text{Mo}_{32}\text{O}_{96}$ of which the

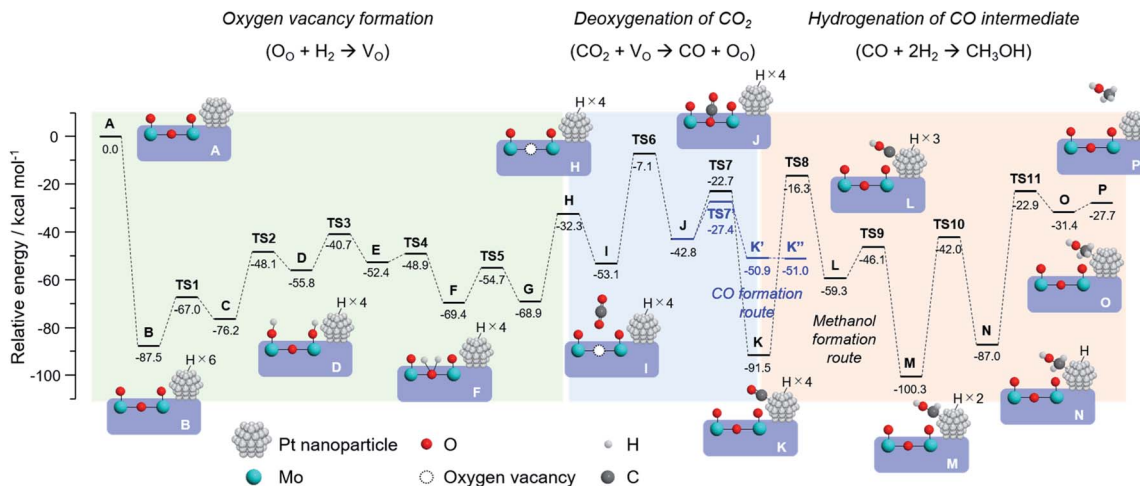


Fig. 8 Optimized reaction pathway for CO_2 hydrogenation to produce methanol, and potential energy diagram obtained by DFT calculation using $\text{H}_{26}\text{Mo}_{32}\text{O}_{96}$ - Pt_{20} slab model and schematic illustrations of the corresponding structure models in each reaction step.

interface is bridged by four Mo–O–Pt bonds was established (state **A** in Fig. 8). The calculated stepwise energy diagrams for CO_2 hydrogenation to methanol are depicted in Fig. 8 (the optimized structure models for each reaction step are presented in Fig. S11 in ESI†). Note that all the presented intermediate states were optimized after considering multiple possible pathways with the lowest energies. To begin with, three H_2 molecules are adsorbed into the slab model, which results in the formation of six dissociated H atoms on the Pt_{20} cluster resulting in a large stabilization energy due to exothermic process (state **B**). The thus formed active H atoms are transferred to nearby surface terminal O atoms (states **C**, **D**), and then coordinated to the bi-bridging oxygen atom (states **E**, **F**), which eventually leads to the formation of H_2O (state **G**) and an oxygen vacancy (state **H**) ($2\text{H}^+ + 2\text{e}^- + \text{O}_\text{O} \rightarrow \text{H}_2\text{O} + \text{V}_\text{O}$), coinciding well with the previous reports of O vacancy formation on $\alpha\text{-MoO}_3$.^{58,59} The above reaction steps proceed with relatively low activation energies ($\text{TS1} \sim \text{TS5}$; $E_a < 28 \text{ kcal mol}^{-1}$) compared with the later reaction steps, while no possible pathways were found over a $\text{H}_{30}\text{Mo}_{32}\text{O}_{96}$ slab model without the Pt_{20} cluster. Thus, an oxygen vacancy is likely to be formed *via* the H-spillover process involving the Pt NPs as illustrated in Scheme 1.

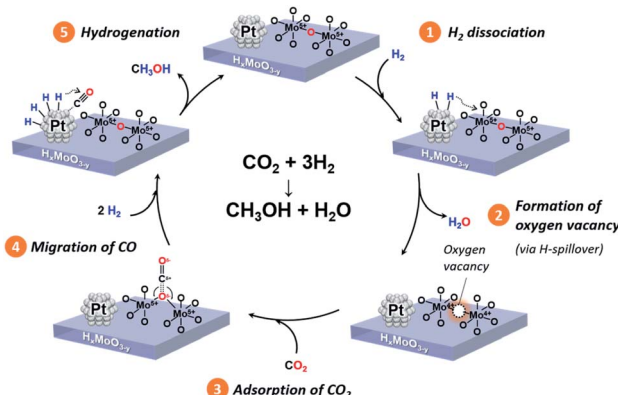
Next, one CO_2 molecule is adsorbed nearby the oxygen vacancy site (state **I**). As demonstrated for the oxygen-defective $\text{H}_{30}\text{Mo}_{32}\text{O}_{95}$ slab model (Fig. 4a), CO_2 is adsorbed and coordinated on the oxygen vacancy (state **J**) with an energy barrier of $46.0 \text{ kcal mol}^{-1}$ (**TS6**) to form the monodentate carbonate species ($^*\text{O-C-O}$) or bidentate carbonate species (CO_3^{2-}) as intermediates, which is well consistent with the results obtained above whereby the oxygen vacancy is responsible for capturing and activating CO_2 . The dissociation of the C=O bond of these intermediates occurs on the O vacancy site with an energy barrier of $20.1 \text{ kcal mol}^{-1}$ (**TS7**), and the dissociated $^*\text{CO}$ is stabilized by being adsorbed on the Pt_{20} cluster (state **K**). The C=O bond cleavage on O vacancy site is corroborated by comparing the reaction paths on the different sites; over the perfect slab model without an oxygen vacancy, CO_2 molecule is stabilized most by being adsorbed on the Pt_{20} cluster surface, and the path for $^*\text{CO}$ formation could not be explored. The

dissociation of CO_2 on the Pt_{20} cluster surface was found to involve a high energy barrier of $102.1 \text{ kcal mol}^{-1}$ (Fig. S12 in ESI†), which is 5-fold higher than that on the O vacancy site, indicating a low possibility of CO_2 dissociation on the Pt surface. Thus, the oxygen vacancy of $\text{H}_x\text{MoO}_{3-y}$ lowers the energy barriers for the cleavage of the C=O bond and functions as a deoxygenation center, rendering the $\text{Pt}/\text{H}_x\text{MoO}_{3-y}$ catalyst highly active towards CO_2 hydrogenation.

Subsequently, the $^*\text{CO}$ intermediate adsorbed on the Pt_{20} cluster is hydrogenated by the active H atoms to finally produce methanol. The H atom on Pt first adds to the oxygen atom of the $^*\text{CO}$ (state **L**), which is followed by successive hydrogenation of the $^*\text{COH}$ intermediate to form $^*\text{CHOH}$ (state **M**), $^*\text{CH}_2\text{OH}$ (state **N**), and finally to produce the desired $^*\text{CH}_3\text{OH}$ (state **O**). The hydrogenation of $^*\text{CO}$ into $^*\text{COH}$, $^*\text{CHOH}$, $^*\text{CH}_2\text{OH}$ and $^*\text{CH}_3\text{OH}$ involves high energy barriers of 75.2 , 13.2 , 58.3 , and $64.1 \text{ kcal mol}^{-1}$, respectively. In particular, the addition of the first H atom to $^*\text{CO}$ is required to overcome the highest energy barrier among all the TS's. This result suggests that CO serves as the main intermediate, and the rate-determining step of this reaction is the hydrogenation of the $^*\text{CO}$ intermediate (**TS8**), this being consistent with the reaction results and the kinetic analysis (Fig. 7).

We further explored the reaction paths for the production of CO and methane over the same slab model. Free CO can be formed from the $^*\text{O-C-O}$ intermediate with an energy barrier of $15.4 \text{ kcal mol}^{-1}$ (**TS7**) (for optimized structure models, see Fig. S13 in ESI†), which is slightly lower than the energy barrier for the formation of the $^*\text{CO}$ intermediate adsorbed on the Pt_{20} cluster (**TS7**: $E_a = 15.4 \text{ kcal mol}^{-1}$) and is significantly lower than those for methanol production from the $^*\text{CO}$ intermediate (**TS8**, **TS10**, **TS11**). This result indicates that gaseous CO formation is thermodynamically more favorable than the formation of methane, being in line with the experimental results. Regarding methane production *via* hydrogenation of the $^*\text{CO}$ intermediate, possible intermediates and reaction pathways over the $\text{H}_{26}\text{Mo}_{32}\text{O}_{96}$ – Pt_{20} model were screened for. Given that the energy barrier for dehydration of $^*\text{CHOH}$ to form $^*\text{CH}$ ($E_a = 65.4 \text{ kcal mol}^{-1}$) was lower than those for dehydration of $^*\text{COH}$ ($E_a = 67.7 \text{ kcal mol}^{-1}$) and $^*\text{CH}_2\text{OH}$ ($E_a = 118.3 \text{ kcal mol}^{-1}$), $^*\text{CH}$ is considered as the stable intermediate upon the formation of methane on the $\text{Pt}/\text{H}_x\text{MoO}_{3-y}$ catalyst (Fig. S14 in ESI†). The following hydrogenation of $^*\text{CH}$ proceeds *via* a stepwise formation of $^*\text{CH}_2$, $^*\text{CH}_3$ and CH_4 with reaction barriers of 20.1 , 36.2 and $54.8 \text{ kcal mol}^{-1}$, respectively. The highest energy barrier to generate methanol from the $^*\text{CHOH}$ intermediate is $64.1 \text{ kcal mol}^{-1}$, which is lower than that for the transformation into methane ($E_a = 65.4 \text{ kcal mol}^{-1}$). Thus, methanol formation is energetically more favorable than methane formation over the $\text{Pt}/\text{H}_x\text{MoO}_{3-y}$ catalyst; hence the higher selectivity for methanol rather than for methane being well elucidated as demonstrated in the reaction experiments.

Based on comprehensive analyses of the reactions, *in situ* spectroscopic measurements and DFT calculations, we conclude that CO_2 hydrogenation to produce methanol over the $\text{Pt}/\text{H}_x\text{MoO}_{3-y}$ catalyst is achieved *via* oxygen vacancy-mediated “reverse Mars–van Kreveren” mechanism,^{31,33,41,72} as illustrated



Scheme 2 Proposed reaction mechanism of CO_2 hydrogenation to produce methanol over the $\text{Pt}/\text{H}_x\text{MoO}_{3-y}$ catalyst.



in Scheme 2. First, oxygen vacancies are formed in the H_xMoO_{3-y} sub-oxide during H_2 reduction through H_2 dissociation on the Pt NPs and the H-spillover process (steps 1 and 2). CO_2 is adsorbed on the oxygen vacancies and activated by the adjacent under-coordinated low-valence Mo centers (Mo^{5+}/Mo^{4+}) *via* electron donation with high adsorption energy, which induces the polarization of CO_2 , weakening and then dissociation of the $C=O$ bond. As a result, a CO intermediate is formed, and the oxygen vacancy is concurrently replenished with O atoms to restore an intact oxide surface (step 3). Based on the exploration by DFT calculation, the *CO intermediate is likely to migrate onto the Pt NP surface (step 4). The *CO intermediate reacts with active H species dissociated on the Pt NPs to initially form *COH species, which then undergo stepwise C–H bond formation, finally leading to the formation of methanol (step 5). A sole H_xMoO_{3-y} works as a “reductant” but cannot be deemed as a “catalyst” for CO_2 reduction. On the contrary, the hybrid Pt/ H_xMoO_{3-y} catalyst developed in this study contains Pt NPs, which act as (i) active sites to supply dissociated H atoms to generate oxygen vacancies in Mo oxide and as (ii) active sites for hydrogenation of the CO intermediate to finally produce methanol (and methane). Owing to the high H_2 dissociation ability of the Pt NP (which occurs at around $140\text{ }^\circ\text{C}$, see Fig. 3a), the catalyst can sustain oxygen vacancies, and thus the catalytic cycle can be realized (steps 1 and 2). These catalytic cycles and the cooperative effect at the Pt– H_xMoO_{3-y} interface facilitate efficient CO_2 hydrogenation under relatively mild reaction conditions.^{38,74,75} The proposed reaction mechanism is totally different from the one known for the conventional Cu-based catalysts which normally require much higher reaction temperatures.^{39,45,46}

In addition, recyclability of the Pt/ H_xMoO_{3-y} (300) catalyst was investigated in recycling tests (Fig. S15 in ESI†). The Pt/ H_xMoO_{3-y} (300) retained its catalytic activity for methanol production over multiple cycles; however, a continuous reduction of activity and methanol yield was observed. Characterization data including the XRD, XPS and XAFS results demonstrated that the structural variation of the H_xMoO_{3-y} support was negligible even after the fourth cycle (see Fig. S16 in ESI†); however, TEM observation showed that the average Pt particle diameter of the spent catalyst apparently increased. As demonstrated above, the CO_2 deoxygenation is the dominant reaction at the interface between the Pt NPs and the H_xMoO_{3-y} sub-oxide. Therefore, the reason for the continuous reduction in activity is probably due to the decreased number of Pt– H_xMoO_{3-y} interfacial sites due to the aggregation of the Pt NPs upon catalytic use,⁷⁸ hence making the cooperative effect less effective.

Conclusions

In conclusion, the Pt/ H_xMoO_{3-y} hybrid catalyst was demonstrated to function as an efficient catalyst for CO_2 hydrogenation to produce methanol under relatively mild reaction conditions. The Pt NPs immobilized on a quasi-stable H_xMoO_{3-y} sub-oxide exhibited the highest CO_2 conversion and methanol yield among the oxide-supported Pt catalysts

examined, with a methanol formation rate of $1.53\text{ mmol g}^{-1}\text{ h}^{-1}$ in the liquid-phase CO_2 hydrogenation under relatively mild reaction conditions (total 4.0 MPa , $200\text{ }^\circ\text{C}$). Comprehensive analyses revealed that abundant surface oxygen vacancies and redox ability of Mo species in quasi-stable H_xMoO_{3-y} endows this catalyst with enhanced adsorption and activation of CO_2 to produce a CO intermediate. As a result, the Pt NP can act as (i) a hydrogenation center to produce methanol from *CO species and as (ii) a site to supply active H atoms to regenerate oxygen vacancies *via* the H-spillover process. Thus, it has been clarified that CO_2 hydrogenation on the Pt/ H_xMoO_{3-y} catalyst is governed by the oxygen-vacancy-mediated “reverse Mars–van Krevelen” mechanism, which is promoted by the synergistic interaction between reducible Mo oxide as a CO_2 -activation center and Pt NP as a H_2 -activation center. For future development with the aim of large-scale implementation, further efforts to improve the reusability as well as to reduce the cost of the catalyst/process are needed. We expect that a continuous production of methanol/CO with a higher methanol selectivity is possible by employing a gas-phase fixed-bed reactor system, which can circumvent some problems in liquid-phase batch reactor system, such as catalyst deactivation, solvent use and post-separation process. The insights gained in this study is expected to provide a new avenue for manipulating catalytic properties *via* “oxygen vacancy engineering” approach and for advancing the mechanistic understanding of heterogeneous catalysis involving oxygen vacancies of metal oxides, which would contribute to the future development of more elaborated and high-performance catalysts for CO_2 hydrogenation.

Author contributions

Y. Kuwahara led the conceptualization, design of the experiments, analysis and validation of the results, and wrote the manuscript. T. Mihogi, K. Hamahara and K. Kusu contributed to material synthesis, data collection, and formal analysis. H. H. Kobayashi contributed to the DFT calculation, formal analysis and data curation. H. Yamashita provided key advice and supervised the study.

Conflicts of interest

There are no conflicts to declare.

Acknowledgements

The present work was supported by JST, PRESTO (grant no. JPMJPR19T3), Japan, the Tonen General Sekiyu Research/Development Encouragement & Scholarship Foundation, and the Iwatani Naoyi Foundation. A part of this work was supported by the grant for research of the Japan Petroleum Institute, 2018, awarded to Y. K. Y. K. and H. Y. thank Element Strategy Initiative of MEXT (grant no. JPMXP0112101003). The synchrotron radiation experiments for XAFS measurements were performed at the BL01B1 beam line in SPring-8 with the approval from JASRI (no. 2018B1185 and 2019A1050).

Notes and references

1 J. Artz, T. E. Muller, K. Thenert, J. Kleinekorte, R. Meys, A. Sternberg, A. Bardow and W. Leitner, *Chem. Rev.*, 2018, **118**, 434–504.

2 A. J. Hunt, E. H. Sin, R. Marriott and J. H. Clark, *ChemSusChem*, 2010, **3**, 306–322.

3 E. V. Kondratenko, G. Mul, J. Baltrusaitis, G. O. Larrazábal and J. Pérez-Ramírez, *Energy Environ. Sci.*, 2013, **6**, 3112–3135.

4 E. A. Quadrelli, G. Centi, J. L. Duplan and S. Perathoner, *ChemSusChem*, 2011, **4**, 1194–1215.

5 A. Alvarez, A. Bansode, A. Urakawa, A. V. Bavykina, T. A. Wezendonk, M. Makkee, J. Gascon and F. Kapteijn, *Chem. Rev.*, 2017, **117**, 9804–9838.

6 M. D. Porosoff, B. Yan and J. G. Chen, *Energy Environ. Sci.*, 2016, **9**, 62–73.

7 R. Sun, Y. Liao, S.-T. Bai, M. Zheng, C. Zhou, T. Zhang and B. F. Sels, *Energy Environ. Sci.*, 2021, **14**, 1247–1285.

8 A. Karelovic, G. Galdames, J. C. Medina, C. Yévenes, Y. Barra and R. Jiménez, *J. Catal.*, 2019, **369**, 415–426.

9 R. P. Ye, J. Ding, W. Gong, M. D. Argyle, Q. Zhong, Y. Wang, C. K. Russell, Z. Xu, A. G. Russell, Q. Li, M. Fan and Y. G. Yao, *Nat. Commun.*, 2019, **10**, 5698.

10 Z. Ma and M. D. Porosoff, *ACS Catal.*, 2019, **9**, 2639–2656.

11 D. R. Palo, *Chem. Rev.*, 2007, **107**, 3992–4021.

12 K. C. Waugh, *Catal. Lett.*, 2012, **142**, 1153–1166.

13 M. Saito, *Catal. Surv. Jpn.*, 1998, **2**, 175–184.

14 G. A. Olah, *Angew. Chem., Int. Ed.*, 2013, **52**, 104–107.

15 G. A. Olah, A. Goeppert and G. K. S. Prakash, *J. Org. Chem.*, 2009, **74**, 487–498.

16 R. Gaikwad, A. Bansode and A. Urakawa, *J. Catal.*, 2016, **343**, 127–132.

17 W. H. Wang, Y. Himeda, J. T. Muckerman, G. F. Manbeck and E. Fujita, *Chem. Rev.*, 2015, **115**, 12936–12973.

18 Y. Chen, S. Choi and L. T. Thompson, *ACS Catal.*, 2015, **5**, 1717–1725.

19 S. Kar, A. Goeppert, J. Kothandaraman and G. K. S. Prakash, *ACS Catal.*, 2017, **7**, 6347–6351.

20 J. Kothandaraman, A. Goeppert, M. Czaun, G. A. Olah and G. K. Prakash, *J. Am. Chem. Soc.*, 2016, **138**, 778–781.

21 N. M. Rezayee, C. A. Huff and M. S. Sanford, *J. Am. Chem. Soc.*, 2015, **137**, 1028–1031.

22 S. Wesselbaum, V. Moha, M. Meuresch, S. Brosinski, K. M. Thenert, J. Kothe, T. V. Stein, U. Englert, M. Holscher, J. Klankermayer and W. Leitner, *Chem. Sci.*, 2015, **6**, 693–704.

23 S. Bai, Q. Shao, Y. Feng, L. Bu and X. Huang, *Small*, 2017, **13**, 1604311.

24 M. U. Khan, L. Wang, Z. Liu, Z. Gao, S. Wang, H. Li, W. Zhang, M. Wang, Z. Wang, C. Ma and J. Zeng, *Angew. Chem., Int. Ed.*, 2016, **55**, 9548–9552.

25 H. Li, L. Wang, Y. Dai, Z. Pu, Z. Lao, Y. Chen, M. Wang, X. Zheng, J. Zhu, W. Zhang, R. Si, C. Ma and J. Zeng, *Nat. Nanotechnol.*, 2018, **13**, 411–417.

26 T. Toyao, S. Kayamori, Z. Maeno, S. M. A. H. Siddiki and K.-i. Shimizu, *ACS Catal.*, 2019, **9**, 8187–8196.

27 Z. He, Q. Qian, J. Ma, Q. Meng, H. Zhou, J. Song, Z. Liu and B. Han, *Angew. Chem., Int. Ed.*, 2016, **55**, 737–741.

28 X. Zheng, Y. Lin, H. Pan, L. Wu, W. Zhang, L. Cao, J. Zhang, L. Zheng and T. Yao, *Nano Res.*, 2018, **11**, 2357–2365.

29 W. Zhang, L. Wang, H. Liu, Y. Hao, H. Li, M. U. Khan and J. Zeng, *Nano Lett.*, 2017, **17**, 788–793.

30 K. W. Ting, T. Toyao, S. M. A. H. Siddiki and K.-i. Shimizu, *ACS Catal.*, 2019, **9**, 3685–3693.

31 D. Ferri, T. Bürgi and A. Baiker, *Phys. Chem. Chem. Phys.*, 2002, **4**, 2667–2672.

32 G. Zhuang, Y. Chen, Z. Zhuang, Y. Yu and J. Yu, *Sci. China Mater.*, 2020, **63**, 2089–2118.

33 L. F. Bobadilla, J. L. Santos, S. Ivanova, J. A. Odriozola and A. Urakawa, *ACS Catal.*, 2018, **8**, 7455–7467.

34 B. J. Hare, D. Maiti, Y. A. Daza, V. R. Bhethanabotla and J. N. Kuhn, *ACS Catal.*, 2018, **8**, 3021–3029.

35 J. Ye, C. Liu, D. Mei and Q. Ge, *ACS Catal.*, 2013, **3**, 1296–1306.

36 G. Xi, S. Ouyang, P. Li, J. Ye, Q. Ma, N. Su, H. Bai and C. Wang, *Angew. Chem., Int. Ed.*, 2012, **51**, 2395–2399.

37 J. Li, Y. Ye, L. Ye, F. Su, Z. Ma, J. Huang, H. Xie, D. E. Doronkin, A. Zimina, J.-D. Grunwaldt and Y. Zhou, *J. Mater. Chem. A*, 2019, **7**, 2821–2830.

38 J. A. Rodriguez, P. Liu, D. J. Stacchiola, S. D. Senanayake, M. G. White and J. G. Chen, *ACS Catal.*, 2015, **5**, 6696–6706.

39 K. Larmier, W. C. Liao, S. Tada, E. Lam, R. Verel, A. Bansode, A. Urakawa, A. Comas-Vives and C. Coperet, *Angew. Chem., Int. Ed.*, 2017, **56**, 2318–2323.

40 M. S. Frei, C. Mondelli, R. Garcia-Muelas, K. S. Kley, B. Puertolas, N. Lopez, O. V. Safonova, J. A. Stewart, D. Curulla Ferre and J. Perez-Ramirez, *Nat. Commun.*, 2019, **10**, 3377.

41 Y. Kuwahara, Y. Yoshimura, K. Haematsu and H. Yamashita, *J. Am. Chem. Soc.*, 2018, **140**, 9203–9210.

42 L. Chen, A. C. Cooper, G. P. Pez and H. Cheng, *J. Phys. Chem. C*, 2008, **112**, 1755–1758.

43 H. Cheng, L. Chen, A. C. Cooper, X. Sha and G. P. Pez, *Energy Environ. Sci.*, 2008, **1**, 338–354.

44 H. Cheng, T. Kamegawa, K. Mori and H. Yamashita, *Angew. Chem., Int. Ed.*, 2014, **53**, 2910–2914.

45 P. Liu, Y. Yang and M. G. White, *Surf. Sci. Rep.*, 2013, **68**, 233–272.

46 S. Kattel, P. Liu and J. G. Chen, *J. Am. Chem. Soc.*, 2017, **139**, 9739–9754.

47 J. J. Birtill and P. G. Dickens, *Mater. Res. Bull.*, 1978, **13**, 311–316.

48 S. Adams, *J. Solid State Chem.*, 2000, **149**, 75–87.

49 B. Braïda, S. Adams and E. Canadell, *Chem. Mater.*, 2005, **17**, 5957–5969.

50 N. A. Chernova, M. Roppolo, A. C. Dillon and M. S. Whittingham, *J. Mater. Chem.*, 2009, **19**, 2526–2552.

51 X. W. Lou and H. C. Zeng, *Chem. Mater.*, 2002, **14**, 4781–4789.

52 P. A. Sermon and G. C. Bond, *Catal. Rev.*, 1973, **8**, 211–239.

53 S. Masuda, K. Shun, K. Mori, Y. Kuwahara and H. Yamashita, *Chem. Sci.*, 2020, **11**, 4194–4203.

54 P. A. Sermon and G. C. Bond, *J. Chem. Soc., Faraday Trans. 1*, 1976, **72**, 730–744.



55 R. Erre, H. van Damme and J. J. Fripiat, *Surf. Sci.*, 1983, **127**, 48–68.

56 R. Erre, H. van Damme and J. J. Fripiat, *Surf. Sci.*, 1983, **127**, 69–82.

57 J. G. Kim and J. R. Regalbuto, *J. Catal.*, 1993, **139**, 175–190.

58 Y.-H. Lei and Z.-X. Chen, *J. Phys. Chem. C*, 2012, **116**, 25757–25764.

59 J. Z. Ou, J. L. Campbell, D. Yao, W. Włodarski and K. Kalantar-zadeh, *J. Phys. Chem. C*, 2011, **115**, 10757–10763.

60 M. Vasilopoulou, A. M. Douvas, D. G. Georgiadou, L. C. Palilis, S. Kennou, L. Sygellou, A. Soultati, I. Kostis, G. Papadimitropoulos, D. Davazoglou and P. Argitis, *J. Am. Chem. Soc.*, 2012, **134**, 16178–16187.

61 H. Cheng, M. Wen, X. Ma, Y. Kuwahara, K. Mori, Y. Dai, B. Huang and H. Yamashita, *J. Am. Chem. Soc.*, 2016, **138**, 9316–9324.

62 H. Cheng, X. Qian, Y. Kuwahara, K. Mori and H. Yamashita, *Adv. Mater.*, 2015, **27**, 4616–4621.

63 H. S. Kim, J. B. Cook, H. Lin, J. S. Ko, S. H. Tolbert, V. Ozolins and B. Dunn, *Nat. Mater.*, 2017, **16**, 454–460.

64 A. Borgschulte, O. Sambalova, R. Delmelle, S. Jenatsch, R. Hany and F. Nuesch, *Sci. Rep.*, 2017, **7**, 40761.

65 J. J. Birtill and P. G. Dickens, *J. Solid State Chem.*, 1979, **29**, 367–372.

66 N. Sotani, K. Eda, M. Sadamitu and S. Takagi, *Bull. Chem. Soc. Jpn.*, 1989, **62**, 903–907.

67 S. Chen, H. Wang, Z. Kang, S. Jin, X. Zhang, X. Zheng, Z. Qi, J. Zhu, B. Pan and Y. Xie, *Nat. Commun.*, 2019, **10**, 788.

68 X. Yang, S. Wang, N. Yang, W. Zhou, P. Wang, K. Jiang, S. Li, H. Song, X. Ding, H. Chen and J. Ye, *Appl. Catal., B*, 2019, **259**, 118088.

69 R. Radhakrishnan, C. Reed, S. T. Oyama, M. Seman, J. N. Kondo, K. Domen, Y. Ohminami and K. Asakura, *J. Phys. Chem. B*, 2001, **105**, 8519–8530.

70 Y. N. Zhou, J. Ma, E. Hu, X. Yu, L. Gu, K. W. Nam, L. Chen, Z. Wang and X. Q. Yang, *Nat. Commun.*, 2014, **5**, 5381.

71 P. Mars and D. W. van Krevelen, *Chem. Eng. Sci.*, 1954, **3**, 41–59.

72 A. V. Mironenko and D. G. Vlachos, *J. Am. Chem. Soc.*, 2016, **138**, 8104–8113.

73 S. Gaur, H. Wu, G. G. Stanley, K. More, C. S. S. R. Kumar and J. J. Spivey, *Catal. Today*, 2013, **208**, 72–81.

74 Y. F. Li, W. Lu, K. Chen, P. Duchesne, A. Jelle, M. Xia, T. E. Wood, U. Ulmer and G. A. Ozin, *J. Am. Chem. Soc.*, 2019, **141**, 14991–14996.

75 Y. F. Li, N. Soheilnia, M. Greiner, U. Ulmer, T. Wood, A. A. Jelle, Y. Dong, A. P. Yin Wong, J. Jia and G. A. Ozin, *ACS Appl. Mater. Interfaces*, 2019, **11**, 5610–5615.

76 S. Bai, Q. Shao, P. Wang, Q. Dai, X. Wang and X. Huang, *J. Am. Chem. Soc.*, 2017, **139**, 6827–6830.

77 A. Lubezky, L. Chechelnitsky and M. Folman, *J. Chem. Soc., Faraday Trans.*, 1996, **92**, 2269–2274.

78 H. Bahruji, M. Bowker, G. Hutchings, N. Dimitratos, P. Wells, E. Gibson, W. Jones, C. Brookes, D. Morgan and G. Lalev, *J. Catal.*, 2016, **343**, 133–146.

